

大视场马赫-曾德尔空间相移双成像系统

孙方圆, 吴双乐, 谢昊天, 闫佩正, 赵琪涵, 王永红*

合肥工业大学仪器科学与光电工程学院, 安徽 合肥 230009

摘要 在基于马赫-曾德尔剪切散斑的干涉双成像系统中, 剪切量的大小方向与空间载波大小方向可独立调节。系统在一个较小剪切量下有较大空间载波, 检测质量较高。在传统马赫-曾德尔双成像系统中, 相机的成像透镜放置在剪切系统后部, 测量视场受剪切系统中第一块分光棱镜尺寸的限制, 视场较小, 效率较低。针对该问题, 介绍了一种改进的空间相移马赫-曾德尔双成像系统。该系统将成像透镜放置在马赫-曾德尔剪切系统的前部, 保留了双成像系统原有的剪切量与载波独立调节的优势, 同时扩大了视场, 提高了检测效率。对内含缺陷的被测物进行测量, 证明了系统可用于缺陷检测。实验证明了可以通过更换成像透镜来改变该系统的视场, 并与传统马赫-曾德尔双成像系统进行了对比, 结果显示所提系统的视场较大。

关键词 测量; 马赫-曾德尔; 空间相移; 大视场; 载波独立调节; 散斑; 干涉

中图分类号 TN247 **文献标志码** A

doi: 10.3788/CJL202148.0704001

1 引言

复合材料由于具有比强度和比模量高、耐疲劳性高等优势, 被广泛应用于航空航天、船舶、车辆等领域^[1-2]。在生产与使用过程中, 复合材料内部常会出现分层、气泡、脱黏等缺陷^[3], 这些缺陷可能会对材料性能产生不良影响, 导致事故发生。剪切散斑干涉技术^[4-5]由于其检测速度快、全场灵敏度高以及对材料种类无特殊要求的优势, 被应用于复合材料的内部缺陷检测, 可以快速高效地测量出材料内部的气泡、分层等缺陷^[6-7]。剪切散斑干涉技术利用携带被测物表面信息的激光, 在经过分光系统后, 实现自干涉并在 CCD 相机靶面成像。相较于散斑干涉技术, 剪切散斑干涉技术更不易受到外界环境的干扰, 在工业环境中有着较好的应用。

当对内部有缺陷的物体进行热加载或者真空加载等处理时, 其内部的缺陷处将会产生与周围无缺陷部分不同的异常变形情况^[8-9], 这种异常变形将会导致被测物表面有异常的变化。通过检测被测物表面的光强或相位分布变化信息^[10], 可以检测出内部有缺陷的区域^[11]。常见的信息处理方法主要有两种: 强度法和相移法^[12-13]。强度法非

常简单而且计算速度快, 但得到的灰度图对比度较差。一些较小或者较深的缺陷经常会被忽略, 从而导致缺陷漏检。相移法主要分为时间相移技术^[14]和空间相移技术^[15]。时间相移技术得到的相位条纹图对比度好, 对被测物内部缺陷较为敏感。但该方法需要在被测物静止的情况下多次引入相移并进行采集, 因此在工业检测中有一定的局限性。空间相移的方法可以被分为多频空间相移技术和空间载波相移技术。前者由于其光路较为复杂, 调试困难, 应用较少。空间载波技术针对相互干涉的两束光, 通过在光路系统中的不同空间位置同时引入相移^[16], 并对 CCD 相机采集到的干涉图进行傅里叶变换和频谱提取, 计算得到物体表面的相位分布信息。空间载波技术只需分别采集加载前后被测物的一幅图, 即可计算出相位分布信息, 简单方便, 可应用于快速检测并获取一系列物体表面变化的相位信息^[17-18]。

在冯家亚^[19]提出的迈克耳孙空间相移系统中, 剪切量与载波均由反射镜引入。为了获得分离的频谱图, 需要较大的剪切量, 但这会使有效测量区域减小。在 Gao 等^[20]提出的马赫-曾德尔双成像系统中, 实现了剪切量和载波的独立调节。成像透镜

收稿日期: 2020-09-01; 修回日期: 2020-09-27; 录用日期: 2020-10-14

*E-mail: yhwang@hfut.edu.cn

放置在马赫-曾德尔剪切系统后,测量面积受到剪切系统第一块分光棱镜尺寸的限制,当系统与被测物距离固定时,系统的视场通常较小。

为了保留剪切量和载波独立调节的优势,同时扩大检测视场,提高检测效率,本文介绍了一种改进的马赫-曾德尔双成像系统,将成像透镜放置在马赫-曾德尔剪切干涉系统前,在系统与被测物距离不

变的情况下扩大了检测视场。对可以产生离面变形和含有内部缺陷的被测物进行测量,验证了该系统可以用于检测离面变形和缺陷。

2 系统原理

大视场马赫-曾德尔空间相移双成像系统的原理图如图 1 所示。

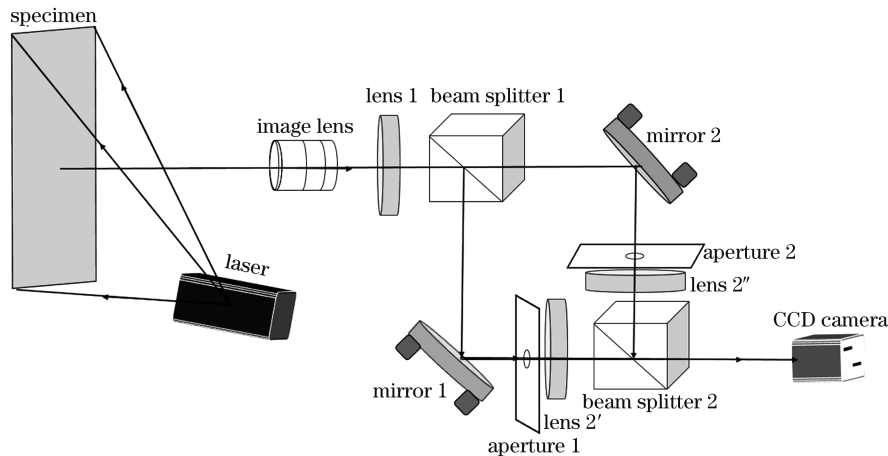


图 1 大视场马赫-曾德尔空间相移双成像系统的原理图

Fig. 1 Principle diagram of Mach-Zehnder-based spatial-phase-shift double-imaging system with large field of view

激光器产生的光经过扩束系统后照射到被测物表面,产生的散斑被具有粗糙表面的被测物反射并经成像透镜成像在其焦平面上。透镜 1 的焦点与成像透镜的焦点重合,因此经过透镜 1 后,被测物表面的光变成了平行光。经过分光棱镜 1 后,两束光分别被反射镜 1 和反射镜 2 反射,其中反射镜 2 引入剪切量。这两束产生剪切量的平行光在经过光阑 1 和光阑 2 时引入了空间载波,这两束平行光分别通过透镜 2' 和透镜 2'' 在 CCD 表面会聚并发生干涉,从而得到散斑干涉图。

光阑 1 与光阑 2 在空间位置上的错位导致空间载波的引入^[21]。当经分光棱镜分束后的两束光分

别通过两个光阑后,相机前的分光棱镜将这两束光重新合并,使其在 CCD 靶面发生干涉。当两个光阑均位于系统的光轴中心时,分别经过两个光阑的光将在空间上有着相同的空间位置信息。当两个光阑相对于光轴中心有错位时,分别经过这两个光阑的光将在空间上有着不同的空间位置信息,这样两束光在相机表面发生干涉后,可以通过对相机采集的图像进行傅里叶变换,并利用之前引入的不同空间位置信息,将含有被测物表面信息的部分与无关信号分离。图 2 展示了两光阑错位引入载波的原理。光阑 1 和光阑 2 对称分布在光阑平面上 O 点的两侧,两束光分别经过光阑 1 和光阑 2 并在 CCD 平面上

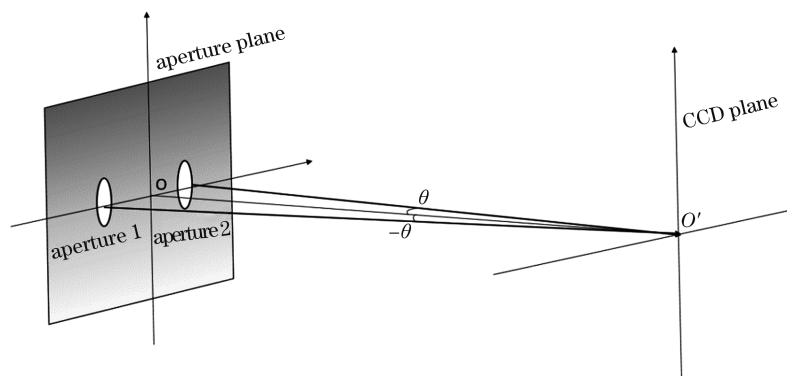


图 2 空间载波引入原理图

Fig. 2 Principle diagram of introduction of spatial carrier frequency

的 O' 点聚焦。通过两个光阑的光与 OO' 的连线夹角分别为 θ 和 $-\theta$ 。当两光阑间的距离改变而光阑平面到 CCD 平面的距离不变时, θ 的值会相应发生变化, 此时载波大小也会发生改变。

载波大小与两光阑间的相对位置的关系为 $f = \frac{\sin \theta}{\lambda}$, 其中 f 是通过光阑的光引入的载波频率, λ 是通过该光阑的光的波长。由此可以看出, 在一个确定的系统中, 由于通过光阑的光波长以及系统中其他器件相对位置不变, 引入的载波大小与光阑间的相对距离有关, 而与其他量无关。

由于成像透镜放置在剪切系统的前方, 因此测量系统的视场将主要受成像透镜的视场限制。相较于传统的双成像系统, 本文提出的大视场双成像系统可以通过改变成像镜头的焦距来调整视场。

在实验上, 可以通过调整反射镜的偏转来引入剪切量。在剪切方向被调制成任意方向的情况下, 推导方法和结果都是相同的。同样, 载波方向被调制成任意方向对推导方法和结果也是无影响的。下面用 x 方向的剪切与 x 方向的频谱为例进行推导。

被测物表面产生的散斑图经过分光棱镜 1 后,

两束光分别被两反射镜反射, 成为相互剪切的光:

$$U_{0,1} = a_1(x, y) \exp[i \cdot \varphi(x, y)], \quad (1)$$

$$U_{0,2} = a_2(x + \Delta x, y) \exp[i \cdot \varphi(x + \Delta x, y)], \quad (2)$$

式中: $U_{0,1}$ 和 $U_{0,2}$ 为两束光的复振幅; $a_1(x, y)$, $a_2(x + \Delta x, y)$ 分别为两束光的振幅; (x, y) 为观察面的坐标; $\varphi(x, y)$, $\varphi(x + \Delta x, y)$ 分别为两束光的相位值; Δx 为偏转反射镜引入的剪切量。

两光阑中心在光轴中心产生横向错位, 从而引入空间载波, 此时两束光可以表示为

$$U_{1,1} = a_1(x, y) \exp[i \cdot \varphi(x, y) - 2\pi i \cdot f \cdot x], \quad (3)$$

$$U_{1,2} = a_2(x + \Delta x, y) \times \exp[i \cdot \varphi(x + \Delta x, y) + 2\pi i \cdot f \cdot x], \quad (4)$$

式中: $U_{1,1}$ 和 $U_{1,2}$ 为引入载波后两束光的复振幅分布; x 为观察平面的横坐标; $f = \frac{\sin \theta}{\lambda}$ 是两束光引入的载波频率。

经过透镜 2'、透镜 2'' 及分光棱镜 2 后, 两束光在 CCD 靶面聚焦并发生干涉, 得到的散斑干涉图可以表示为

$$I = (U_{1,1} + U_{1,2})(U_{1,1} + U_{1,2})^* = a_1^2(x, y) + a_2^2(x + \Delta x, y) + a_1(x, y)a_2(x + \Delta x, y) \exp[i \cdot \varphi(x, y) - i \cdot \varphi(x + \Delta x, y) - 4\pi i \cdot f \cdot x] + a_1(x, y)a_2(x + \Delta x, y) \exp[i \cdot \varphi(x, y) - i \cdot \varphi(x + \Delta x, y) + 4\pi i \cdot f \cdot x] \quad (5)$$

式中: I 为相机采集图的光强度分布; $*$ 为共轭。

对(5)式表示的散斑干涉图进行傅里叶变换, 可以得到三个相互分离的部分: $\mathcal{F}[a_1^2(x, y) + a_2^2(x + \Delta x, y)]$, $\mathcal{F}\{a_1(x, y)a_2(x + \Delta x, y) \cdot \exp[i \cdot \varphi(x, y) - i \cdot \varphi(x + \Delta x, y) - 4\pi i \cdot f \cdot x]\}$ 和 $\mathcal{F}\{a_1(x, y)a_2(x + \Delta x, y) \exp[i \cdot \varphi(x, y) - i \cdot \varphi(x + \Delta x, y) + 4\pi i \cdot f \cdot x]\}$ 。其中 $\mathcal{F}[a_1^2(x, y) +$

$a_2^2(x + \Delta x, y)]$ 是背景信息, 不包含被测物表面的相位信息, 位于频谱图中心, 另外两个携带相位信息的频谱对称分布在中心频谱上。携带相位信息的频谱与中心频谱的距离受载波大小的影响。

任意选取两个携带相位信息的频谱中的一个, 再次进行傅里叶变换, 可以得到物体表面相位分布情况:

$$\varphi(x, y) = \varphi(x, y) - \varphi(x + \Delta x, y) = \arctan \frac{\text{Im}[i \cdot \varphi(x, y) - i \cdot \varphi(x + \Delta x, y) - 4\pi i \cdot f \cdot x]}{\text{Re}[i \cdot \varphi(x, y) - i \cdot \varphi(x + \Delta x, y) - 4\pi i \cdot f \cdot x]} \pm 4\pi i \cdot f \cdot x, \quad (6)$$

式中: $\varphi(x, y)$ 为变形前物体表面的相位分布的一阶导数; $\text{Im}(\cdot)$ 表示取虚部; $\text{Re}(\cdot)$ 表示取实部。

对被测物进行顶针加载, 使其表面产生中心凸起的变形。使用相机进行图像采集, 并利用图像处理方式, 得到加载后物体表面相位分布的一阶导数 $\varphi'(x, y)$ 。则被测物表面变形情况可以表示为

$$\Delta\varphi(x, y) = \varphi(x, y) - \varphi'(x, y)。$$

3 实验结果与分析

针对上述原理进行实验验证。实验系统采用直径为 130 mm 的标准顶针加载内部无缺陷被测物, 如图 3(a) 所示。该被测物四周由螺钉固定, 背后采

用螺旋测微头旋转顶针进行加载,加载中心与被测物中心一致。另一块被测物是直径为 80 mm 的内

置缺陷的标准被测物。采用气压加载的方式,被测物内置缺陷的深度大小均不相同,如图 3(b)所示。

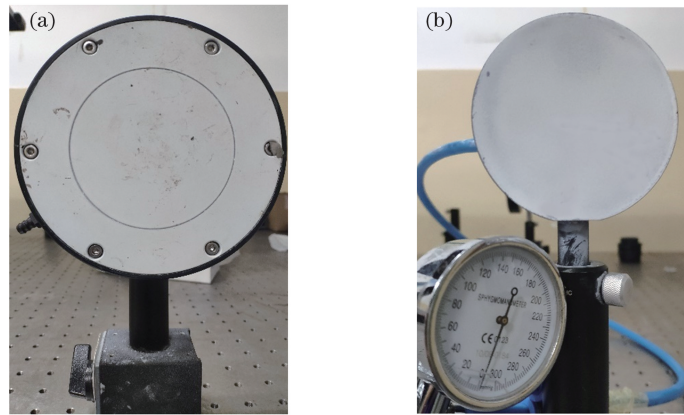


图 3 被测物照片。(a)顶针加载无缺陷被测物;(b)气压加载内置缺陷的被测物

Fig. 3 Picture of object to be measured. (a) Defect-free and thimble-loaded object; (b) defect-built-in and air-pressure-loaded object

组建的大视场双成像系统如图 4 所示。利用面阵工业相机对干涉图进行采集。相机采集帧率为

15 frame/s,曝光时间为 30 ms,成像镜头的焦距为 35 mm。系统中使用的分光棱镜分光比均为 50 : 50。

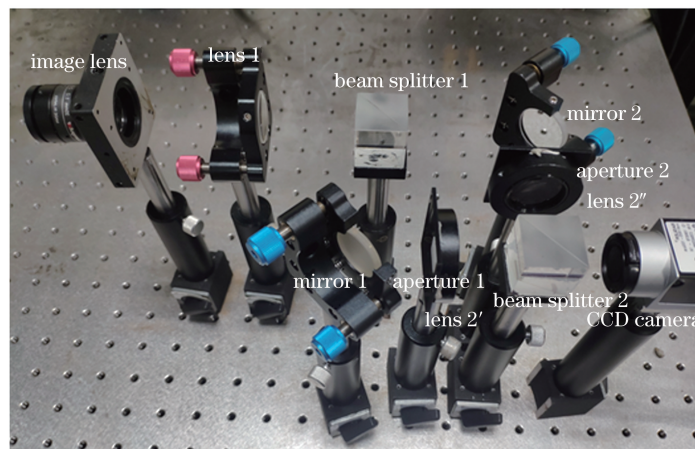


图 4 大视场马赫-曾德尔空间相移双成像系统的光路图

Fig. 4 Light path diagram of Mach-Zehnder-based spatial-phase-shift double-imaging system with large field of view

采用的激光器是功率为 200 mW 的 532 nm 固体激光器。从理论上来说,入射激光的角度与光轴的夹角应该为 0,这样在后续的计算中,取入射光与反射光的夹角 $\alpha=0$,则相关相位变化 Δ_x 与变形量偏导数之间的关系可以由 $\Delta_x = \frac{2\pi\delta x}{\lambda} \times \left[\sin \alpha \frac{\partial u}{\partial x} + (1 + \cos \alpha) \frac{\partial w}{\partial x} \right]$ (此处以 x 方向的位移偏导为例),简化成为 $\Delta_x = \frac{4\pi\delta x}{\lambda} \times \frac{\partial w}{\partial x}$,其中 u 为面内变形量, w 为离面变形量, λ 为激光波长, δx 是系统使用的剪切量值。

然而,在实际情况下,由于光路系统本身具有一

定的尺寸,无法实现 $\alpha=0$,但在 α 较小的情况下, $\sin \alpha \approx 0$,因此近似结论 $\Delta_x = \frac{4\pi\delta x}{\lambda} \times \frac{\partial w}{\partial x}$ 依然成立^[22]。本文在不影响后续测量光路的前提下,将激光器放置在与测量光轴夹角约为 7° 的位置处。

为了获得更好的散斑质量与可分离的频谱,采用的光阑直径为 2 mm,并将两光阑放置在两光阑中心连线与水平面夹角为 45° 的方向上。对相机采集到的散斑干涉图进行傅里叶变换,得到的频谱图如图 5 所示。

对图 5 圆圈区域的频谱进行傅里叶变换,可以得到被测物表面的相位分布图。将被测物变形前后的相位分布进行相减,可以得到被测物表面变形量

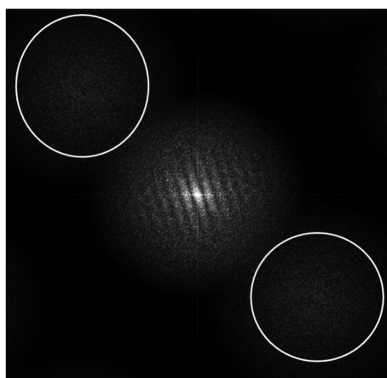


图 5 相机采集到的散斑干涉图的傅里叶变换结果
Fig. 5 Fourier transform result of speckle interference pattern obtained by camera

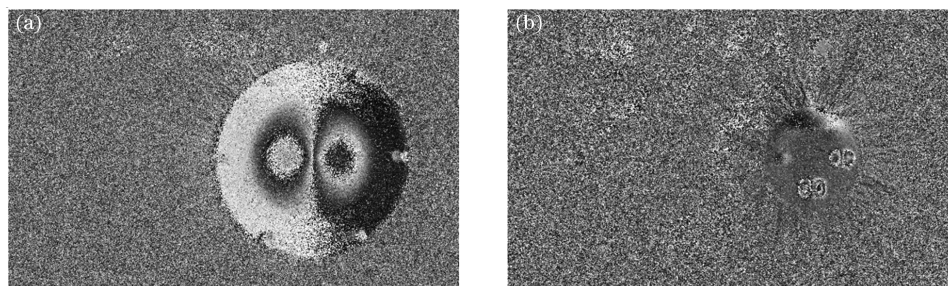


图 6 被测物变形后的相位分布图。(a)顶针加载无缺陷被测物;(b)气压加载内置缺陷的被测物
Fig. 6 Phase distribution maps of object after deformation. (a) Defect-free and thimble-loaded object; (b) defect-built-in and air-pressure-loaded object

为了验证大视场双成像系统在测量范围方面的优势,利用含有不同焦距成像透镜的大视场马赫-曾

的相位分布。

利用图 4 所示的实验系统对两种被测物变形情况进行检测,使用的成像透镜焦距为 35 mm。对被测物加载前后的散斑图进行傅里叶变换,并对频谱图(图 5)中圆圈所标识的两部分频谱中的任意一部分再次进行傅里叶变换。将加载前后的结果进行相减,获得两被测物变形后的结果,如图 6 所示。

从图 6 结果可以看出,大视场马赫-曾德尔双成像系统可以得到较好的被测物离面变形相位分布情况,同时在内置缺陷的被测物测量方面,也有较好的表现。

德尔空间相移双成像系统以及传统马赫-曾德尔双成像系统测量同一被测物,结果如图 7 所示。大视

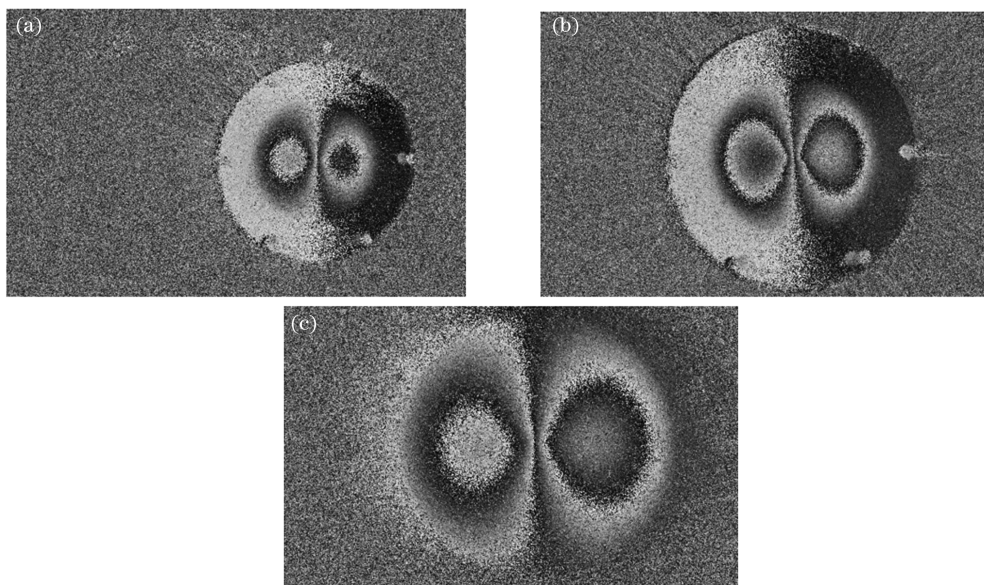


图 7 使用不同焦距成像透镜的所提系统及传统马赫-曾德尔双成像系统的测量结果。(a)含有焦距为 35 mm 成像透镜的所提系统;(b)含有焦距为 50 mm 成像透镜的所提系统;(c)传统马赫-曾德尔双成像系统

Fig. 7 Measurement results of proposed system using imaging lens with different focal lengths and traditional Mach-Zehnder-based spatial-phase-shift double-imaging system. (a) Proposed system including imaging lens with 35 mm focal length; (b) proposed system including imaging lens with 50 mm focal length; (c) traditional Mach-Zehnder-based spatial-phase-shift double-imaging system

场马赫-曾德尔双成像系统使用焦距为 35 mm 和 50 mm 的成像透镜,对被测物进行检测。被测物放置在距离成像透镜约 1.5 m 处。使用焦距为 35 mm 的成像镜头进行测量,实际测量面积约为 300 mm×190 mm,如图 7(a)所示。使用焦距为 50 mm 的成像镜头进行测量,实际测量面积约为 230 mm×140 mm,如图 7(b)所示。传统马赫-曾德尔双成像系统的测量结果如图 7(c)所示,实际测量面积约为 105 mm×65 mm。

从图 7 可以看出,所提系统的测量范围明显大于传统马赫-曾德尔双成像系统的测量范围。同时,所提系统的测量范围受成像透镜的焦距影响,但不再受剪切系统元件尺寸的限制。在传统双成像系统中,视场约为 105 mm×65 mm,而在所提系统中,最小视场约为 230 mm×140 mm,最大视场约为 300 mm×190 mm。由此可以看出,在视场扩大时,被测物面上每个像素对应的面积增大,实际分辨率有所降低。在实际的检测过程中,根据视场需求以及测量质量的要求,应选择大于相机靶面尺寸的短焦镜头以及更高分辨率的相机,在保证检测效率的同时保证检测质量。

4 结 论

介绍了一种基于马赫-曾德尔的大视场空间相移双成像测量系统,将成像透镜放置在剪切系统前部,剪切量通过反射镜进行调节,载波大小通过放置在两透镜前的光阑间的相对位置进行调节。该测量系统可实现剪切量与载波的独立调节,同时可以通过更换具有不同焦距的成像透镜进行视场大小的调整。实验证明了该系统可以应用于离面变形分布和缺陷的检测中,且测量视场可以更大。根据实际需求进行调节,在提高测量效率的同时保证测量质量。

参 考 文 献

- [1] Zhang S Y, Liu J Q, Yu X X, et al. Mechanical properties of composite structures [M]. Beijing: Beijing Institute of Technology Press, 1992.
张双寅,刘济庆,于晓霞,等. 复合材料结构的力学性能[M]. 北京:北京理工大学出版社,1992.
- [2] Li J. Application and development of composite materials for new generation of civil aircraft engines [J]. Aeronautical Science & Technology, 2012, 23(1): 18-22.
李杰. 复合材料在新一代商用发动机上的应用与发展[J]. 航空科学技术, 2012, 23(1): 18-22.

- [3] Ye L, Shen Z, Yang S C, et al. Characterization of damage resistance and damage tolerance behavior of composite laminates [J]. Acta Materialia Composita Sinica, 2003(3): 12-26.
叶林,沈真,杨胜春,等. 复合材料损伤阻抗和损伤容限的性能表征[J]. 结构强度研究, 2003(3): 12-26.
- [4] Hung Y Y. Shearography: A new optical method for strain measurement and nondestructive testing [J]. Optical Engineering, 1982, 21(3): 213391.
- [5] Yang L X, Chen F, Steinchen W, et al. Digital shearography for nondestructive testing: potentials, limitations, and applications [J]. Journal of Holography and Speckle, 2004, 1(2): 69-79.
- [6] Willemann D P, Fantin A, Gonçalves A A Jr. Defect assessment of bonded joints of composite tubes using shearography[J]. SPIE, 2010, 7387: 73870J.
- [7] Wang Y H, Lyu Y B, Gao X Y, et al. Research progress in shearography and its applications [J]. Chinese Optics, 2017, 10(3): 300-309.
王永红,吕有斌,高新亚,等. 剪切散斑干涉技术及应用研究进展[J]. 中国光学, 2017, 10(3): 300-309.
- [8] Ma Y H, Jiang H Y, Dai M L, et al. Cantilevered plate vibration analysis based on electronic speckle pattern interferometry and digital shearing speckle pattern interferometry[J]. Acta Optica Sinica, 2019, 39(4): 0403001.
马银行,蒋汉阳,戴美玲,等. 基于电子散斑干涉与数字剪切散斑干涉法的悬臂薄板振动分析[J]. 光学学报, 2019, 39(4): 0403001.
- [9] Ruzek R, Lohonka R, Jironc J. Ultrasonic C-Scan and shearography NDI techniques evaluation of impact defects identification [J]. NDT & E International, 2006, 39(2): 132-142.
- [10] Gu J W, Xie X P, Cao Y B, et al. A semi-dense depth map acquisition algorithm based on laser speckle[J]. Chinese Journal of Lasers, 2020, 47(3): 0304004.
古家威,谢小鹏,曹一波,等. 基于激光散斑的半稠密深度图获取算法[J]. 中国激光, 2020, 47(3): 0304004.
- [11] Wang T, Li Z, Wang S, et al. Blades model reconstruction based on speckle vision measurement [J]. Laser & Optoelectronics Progress, 2019, 56(1): 011501.
王涛,李战,王盛,等. 基于散斑视觉测量的叶片模型重构[J]. 激光与光电子学进展, 2019, 56(1): 011501.
- [12] Hung Y Y, Tang S, Hovanesian J D. Real-time shearography for measuring time-dependent

- displacement derivatives [J]. *Experimental Mechanics*, 1994, 34(1): 89-92.
- [13] Liu Y X, Wang Y H, Gao X Y, et al. Research on phase measurement technologies in speckle pattern interferometry[J]. *Tool Engineering*, 2016, 50(9): 89-94.
刘莹雪, 王永红, 高新亚, 等. 基于散斑干涉的相位测量技术研究[J]. *工具技术*, 2016, 50(9): 89-94.
- [14] Lü Y B. Design and research of nondestructive testing system based on shearography [D]. Hefei: Hefei University of Technology, 2017.
吕有斌. 基于剪切散斑干涉的无损检测系统设计与研究[D]. 合肥: 合肥工业大学, 2017.
- [15] Liu T C, Wu S J, Li W X. Spatial carrier digital speckle pattern interferometry system with large field of view[J]. *Chinese Journal of Lasers*, 2020, 47(9): 0904001.
刘天承, 吴思进, 李伟仙. 大视场空间载波数字散斑干涉系统[J]. *中国激光*, 2020, 47(9): 0904001.
- [16] Xie X, Yang L, Xu N, et al. Michelson interferometer based spatial phase shift shearography [J]. *Applied Optics*, 2013, 52(17): 4063-4071.
- [17] Zhang H F, Wu S J, Li W X, et al. Full-field measurement of micro deformation of pulsation using spatial-carrier digital speckle pattern interferometry [J]. *Tool Engineering*, 2018, 52(8): 150-153.
张恒飞, 吴思进, 李伟仙, 等. 空间载波数字散斑干涉脉动微变形的全场测量[J]. *工具技术*, 2018, 52(8): 150-153.
- [18] Yan P Z, Liu X W, Wu S L, et al. Pixelated carrier phase-shifting shearography using spatiotemporal low-pass filtering algorithm [J]. *Sensors*, 2019, 19(23): E5185.
- [19] Feng J Y. Research on the spatial carrier shearography based on Machelson interferometer[D]. Hefei: Hefei University of Technology, 2015.
冯家亚. 基于迈克尔逊干涉仪的空间载波剪切散斑干涉技术研究[D]. 合肥: 合肥工业大学, 2015.
- [20] Gao X Y, Wang Y H, Dan X Z, et al. Double imaging Mach-Zehnder spatial carrier digital shearography[J]. *Journal of Modern Optics*, 2019, 66(2): 153-160.
- [21] Bhaduri B, Mohan N K, Kothiyal M P. (1, N) spatial phase-shifting technique in digital speckle pattern interferometry and digital shearography for nondestructive evaluation [J]. *Optical Engineering*, 2007, 46(5): 051009.
- [22] Yang L. Digital shearography: theory and application of digital speckle pattern shearing interferometry [M]. Bellingham: SPIE, 2003.

Mach-Zehnder-Based Spatial-Phase-Shift Double-Imaging System with Large Field of View

Sun Fangyuan, Wu Shuangle, Xie Haotian, Yan Peizheng, Zhao Qihan, Wang Yonghong*

School of Instrument Science and Opto-Electronic Engineering, Hefei University of Technology,

Hefei, Anhui 230009, China

Abstract

Objective Composite materials have the advantages of high specific strength, specific modulus, and fatigue resistance and have been widely used in aerospace, ships, vehicles, and other fields. However, the properties of composites are easily influenced by their internal defects. Shearography has the advantages of full field, high sensitivity, anti-environmental-interference, and no special requirements of material types. Compared with temporal-phase-shift-based shearography, spatial-phase-shift-based shearography has a fast detection speed and is suitable for real-time detection. Spatial carrier frequency introduction is the most commonly used spatial-phase-shift method. However, in the Michelson-based spatial-phase-shift system, the shear amount and spatial phase shift are both controlled by a rotating mirror. To obtain a separated spectral diagram, a large amount of shear is required, but the effective measurement area is reduced, which leads to excessive sensitivity. In the Mach-Zehnder-based spatial-phase-shift double-imaging system proposed by Gao et al., the shear amount and spatial phase shift can be controlled independently. The imaging lens is placed after the Mach-Zehnder shear part, and the detection area of the system is limited by the size of the first beam-splitter prism in the shear part. When the distance between the shearography system and the detected material is fixed, the field of view of the system is usually small and fixed. Because of the small field of view, the detection efficiency is low. To solve this problem, this paper introduces an improved Mach-Zehnder-based spatial-phase-shift double-imaging system. The advantage of the independent adjustment of shear

amount and spatial carrier frequency is retained, the field of view is enlarged, and the detection efficiency is improved.

Methods The solid state laser with a wavelength of 532 nm is expanded by the beam expander and irradiates on the surface of a rough material. The speckle produced by the rough surface of the material is reflected and imaged by an imaging lens on its focal plane. The focal point of lens 1 coincides with that of the imaging lens, so after passing through lens 1, the light reflected by the rough surface becomes parallel light. After passing beam-splitter 1, the two light beams are reflected by mirror 1 and mirror 2, respectively, where mirror 2 is used to introduce shear. The spatial carrier frequency is introduced in the two beams and is generated after passing through apertures 1 and 2. The two beams converge via lens 2' and lens 2'', and after passing through beam-splitter 2, the two light beams interfere with each other on the CCD target; thus, the speckle pattern is obtained. The spatial carrier frequency is introduced by the dislocation of apertures 1 and 2 in the spatial position. When the beam is passing through the aperture, the spatial carrier frequency is introduced into the beam. In a certain system in which the wavelength of laser and the distance between the aperture and CCD camera are fixed, the spatial carrier frequency is influenced only by the spatial positions of the two apertures. After the Fourier transform of the image obtained by the CCD camera, the spectrum with phase information can be separated. The inverse Fourier transform is applied to the spectrum containing the phase information, and the deformation distribution can be obtained by subtracting the phase information before and after the deformation.

Results and Discussions Two specimens were analyzed in this work: a defect-free aluminum plate and a composite plate with internal defects. The Mach-Zehnder-based spatial-phase-shift double-imaging system with a large field of view uses an imaging lens with a focal length of 35 mm to analyze the two specimens. The first derivative of the out-of-plane deformation distribution is shown in Fig. 6(a) and the internal defect distribution can be seen in Fig. 6(b). The result shown in Fig. 6 proves the suitability of the system for surface deformation and defect detection. The same specimen was analyzed using the traditional and Mach-Zehnder-based spatial-phase-shift double-imaging system with a large field of view including two imaging lens with different focal lengths, and Fig. 7 shows the contrast experimental results. From Fig. 7, the double-imaging system has a large field of view compared with the traditional double-imaging system. The use of imaging lenses with different focal lengths can change the field of view. When the camera is unchanged, the enlarged field of view causes the image resolution to decrease. In the actual detection process, according to the field of view and the quality requirements, a camera with higher resolution and a larger target surface and matching short-focal-length imaging lens can be used.

Conclusions This paper introduces a Mach-Zehnder-based spatial-phase-shift double-imaging system with a large field of view that can be used to detect deformation and internal defects. The spatial carrier frequency can be adjusted by changing the relative position of the two apertures placed in front of the lens. The advantage of adjusting spatial carrier frequency and shear amount independently is retained. The experimental results reveal that the field of view in double-imaging shearography can be enlarged by changing the focal length of the imaging lens. According to the actual situation, the field of view is adjustable by changing the focal length of the imaging lens, which leads to an improvement in efficiency.

Key words measurement; Mach-Zehnder; spatial phase shift; large field of view; independent adjustable carrier frequency; speckle; interference

OCIS codes 120.4820;120.6160